Commun. Comput. Phys.
doi: 10.4208/cicp.OA-2024-0292

Vol. **39**, No. 5, pp. 1620-1643
May 2026

A Two-Stage Fourth-Order Gas-Kinetic CPR Method for Subsonic Flows on Hexahedral Meshes

Chao Zhang[1,3], Qibing Li[1,2,*] and Zhihui Li[4]

[1] *AML, Department of Engineering Mechanics, Tsinghua University, Beijing 100084, China.*
[2] *State Key Laboratory of Advanced Space Propulsion, Tsinghua University, Beijing, 100084, China.*
[3] *Beijing Institute of Applied Physics and Computational Mathematics, Beijing 100084, China.*
[4] *China Aerodynamics Research and Development Center, Mianyang 621000, China.*

Received 4 December 2024; Accepted (in revised version) 16 July 2025

Abstract. A compact high-order gas-kinetic scheme (GKS) is developed for three-dimensional subsonic inviscid and viscous flows on hexahedral meshes, which achieves fourth-order accuracy in both space and time. The scheme combines a compact and efficient correction procedure via reconstruction (CPR) framework with a time-evolving gas-kinetic flux, in which the inviscid and viscous fluxes are coupled and computed uniformly. With the CPR framework, the current scheme avoids the difficulty of compact fourth-order reconstruction encountered by the traditional finite volume GKS. Moreover, both the flux and its time-derivative are available in the gas-kinetic flux so that an efficient two-stage temporal discretization can be adopted to achieve fourth-order time accuracy, which is more efficient than the traditional Runge-Kutta CPR method. In addition, with the help of isoparametric transformation, the current scheme can treat curved boundaries with high-order curved meshes. Typical numerical tests demonstrate the good performance of the current scheme.

PACS: 47.55.nb, 47.20.Ky, 47.11.Fg

Key words: Gas-kinetic scheme, correction procedure via reconstruction, two-stage fourth-order temporal discretization, curved mesh.

1 Introduction

In recent years, high-order methods on unstructured meshes have attracted increasing attention in the community of computational fluid dynamics to accurately capture the

*Corresponding author. *Email addresses:* lqb@tsinghua.edu.cn (Q.B. Li), zhangchaoxmu@126.com (C. Zhang), zhli0097@x263.net (Z. Li)

aerodynamic forces and heating on the flying objects with complex geometries [1]. With the same computational cost, high-order methods can achieve higher accuracy and efficiency than second-order methods. A variety of high-order methods have been developed during the past decades, such as the Discontinuous Galerkin (DG) method [2–4], the spectral difference (SD) method [5, 6] and the spectral volume (SV) method [7, 8]. These mentioned methods are characterized by compactness with inner degrees of freedom (IDOFs), when compared with the finite volume (FV) method [9, 10].

In 2007, Huynh proposed a simple and efficient method, named as the flux reconstruction (FR) method [11, 12]. Wang, Gao and Haga et al. extended it to triangular and mixed grids with the name of lifting collocation penalty (LCP) method [13–16]. FR and LCP were also renamed as correction procedure via reconstruction (CPR) [17]. It can recover many typical high-order methods, including DG, SD and SV, by choosing corresponding correction functions, with the advantage of simplicity and efficiency. Achieving high-order accuracy not only depends on high-order discretization of space, but also high-order time-evolution. Riemann solvers for Euler equations are widely used to compute the inviscid flux, while the viscous flux needs to be treated separately. As these traditional flux solvers are usually only first-order time accurate, the multi-stage Runge-Kutta (R-K) methods are usually adopted for high-order time accuracy, except for the ADER solver [18, 19] and the generalized Riemann problem (GRP) solver.

The Bhatnagar-Gross-Krook (BGK) model provides a mesoscopic description of flows through the gas distribution function, which can recover the Naiver-Stokes (N-S) equations by the first-order Chapman-Enskog expansion. Based on the BGK equation, the gas-kinetic scheme (GKS) has been developed [20, 21] and applied in a variety of flows. Its success is attributed to the adoption of the local integral solution of the BGK equation to compute the macroscopic flux, which describes a multiscale evolution from a kinetic scale to a hydrodynamic scale [22]. Thus the flux uniformly couples the inviscid and viscous effects and also contains an adaptive numerical dissipation. More importantly, the flux function is explicitly evolving in both space and time, which guarantees the genuine multidimensionality and makes it possible to use less quadrature points or stages for high-order accuracy [23].

Through a second-order Taylor expansion of the gas distribution function, Li et al. proposed a third-order GKS successfully, which achieves third-order time accuracy within a single stage [24–26]. This method has been extended to a series of framework, such as the compact FV-GKS [27], DG-GKS [28], SV-GKS [29] and CPR-GKS [30]. To achieve high-order time accuracy more efficiently, professor Jiequan Li developed a two-stage fourth-order (S2O4) temporal discretization for the GRP solver with the use of both the flux and its time-derivative [31–33]. It has been extended to the DG framework, which shows higher efficiency than RKDG [34, 35]. It has also been adopted to develop a two-stage fourth-order FV GKS based on the second-order GKS flux [36–39], as the time-derivative is also available. For three-dimensional flows, a compact third-order gas-kinetic scheme has also been developed recently by using the S2O4 time-stepping method [40]. However, for FV GKS, high-order compact reconstruction is still a chal-

lenging work, which only face-neighboring cells are involved in the stencil, especially for fourth-order space accuracy or above. Existing high-order GKS under the traditional FV framework are mainly based on the non-compact WENO reconstruction, or third-order compact reconstruction. Through the subcell finite volume (SCFV) framework, both third-order and fourth-order compact reconstructions have been successfully achieved for high-order GKS on triangular meshes, as well as hexahedral meshes [41–43]. Recently, with the help of S2O4, a fourth-order accurate CPR-GKS has been developed on triangular meshes, which shows higher efficiency for solving viscous flow problems than traditional CPR with the multi-stage R-K method. Besides, as shown in [41], with suitable choice of solution points, CPR-GKS can be more accurate and efficient than SCFV-GKS. Therefore, it is worthwhile to extend this method to 3D meshes for 3D practical flow problems.

In the present study, the two-stage fourth-order CPR-GKS is extended to three-dimensional hexahedral meshes for the Euler and N-S equations. For simplicity, only subsonic flows are considered. The constructed scheme combines the compact and efficient CPR framework with the robust and time-evolving GKS flux. With the CPR framework, it is easier and more straightforward to implement compact fourth-order reconstruction than FV framework. Compared with traditional CPR methods, it obtains the inviscid and viscous fluxes uniformly and achieves fourth-order accuracy in both space and time with only one middle stage. So there is no need to use the R-K method.

For high-order methods, it is critical to treat curved boundaries correctly. If the computational mesh fails to coincide with the real physical boundary, large errors may arise near the boundary and the solutions inside the computational domain may also be polluted. High-order methods, such as DG, CPR, may face even worse situation than the FV methods, since each element contains several IDOFs. Krivodonova and Berger proposed a simple approach based on straight-sided elements to treat curved boundaries [44], which has been adopted by Ji et al. in their recent study [45]. The most popular way to treat curved boundaries is based on high-order isoparametric elements [46] which is more accurate and the conservation can be guaranteed. It can be conveniently applied in the current fourth-order CPR-GKS, under the CPR framework.

The paper is organized as follows. Section 2 introduces the construction of the current method, including the CPR framework, the gas-kinetic flux solver and the two-stage temporal discretization. Numerical tests are presented in Section 3 to validate the performance of the method. The last section draws the conclusions.

2 Numerical method

2.1 CPR framework

The CPR framework on hexahedral meshes can be extended directly from the one-dimensional (1D) FR method via tensor product [11]. Consider the conservation law

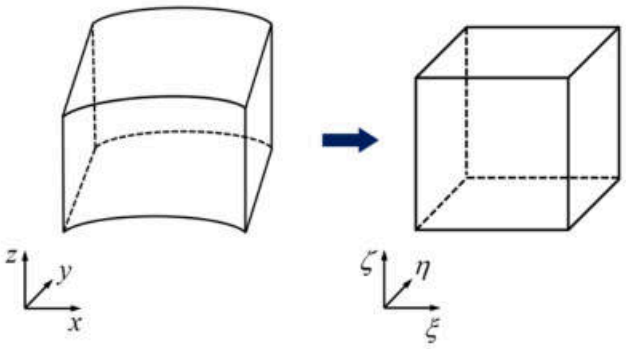

Figure 1: Transformation from a physical element to a standard element.

$$\frac{\partial \mathbf{Q}}{\partial t}+\nabla\cdot\mathbf{F}=\mathbf{0}, \tag{2.1}$$

where $\mathbf{Q}=(\rho,\rho\mathbf{U},\rho E)^T$ are the conservative variables, with macroscopic velocities $\mathbf{U}=(U,V,W)$, and $\mathbf{F}=(\mathbf{F}^x,\mathbf{F}^y,\mathbf{F}^z)$ is the flux vector. The computational domain is divided into N non-overlapping hexahedral elements $\{\Omega_i\}$. To achieve an efficient implementation, each hexahedral element in the physical space $\mathbf{x}=(x,y,z)$ is transformed into the standard element $(\xi,\eta,\zeta)\in[-1,1]\times[-1,1]\times[-1,1]$ in the computational space, as illustrated in Fig. 1. In addition, to handle curved boundaries, cubic isoparametric elements are adopted, which is consistent with the fourth-order space accuracy of the current scheme.

The transformed governing equations in the computational space can be expressed as

$$\frac{\partial \check{\mathbf{Q}}}{\partial t}+\check{\nabla}\cdot\check{\mathbf{F}}=\mathbf{0}, \tag{2.2}$$

where

$$\begin{aligned}
&\check{\mathbf{Q}}=|J|\mathbf{Q},\\
&\check{\mathbf{F}}^{\xi}=|J|(\xi_x\mathbf{F}^x+\xi_y\mathbf{F}^y+\xi_z\mathbf{F}^z),\\
&\check{\mathbf{F}}^{\eta}=|J|(\eta_x\mathbf{F}^x+\eta_y\mathbf{F}^y+\eta_z\mathbf{F}^z),\\
&\check{\mathbf{F}}^{\zeta}=|J|(\zeta_x\mathbf{F}^x+\zeta_y\mathbf{F}^y+\zeta_z\mathbf{F}^z),
\end{aligned} \tag{2.3}$$

in which ξ_x, ξ_y, ξ_z, et al. are the components of the inverse of the Jacobian matrix J.

Inside each element, $k+1$ solution points are set along each coordinate direction so that the 1D Lagrange polynomial with degree k can be constructed, and there are $(k+1)^3$ SP in total. For fourth-order space accuracy, we set $k=3$. The Gauss point is chosen for SP and the distribution in the $\xi-\eta$ plane of a standard element is shown in Fig. 2, in which the flux points for the common flux are also presented. The distribution along the ζ direction is similar. For brevity, solution point and flux point are abbreviated as SP and FP respectively in the following.

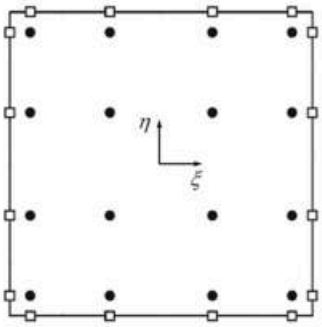

Figure 2: Distribution of solution points (circle) and flux points (square) along ξ and η directions in the standard element with k=3.

Denoting $\breve{\mathbf{Q}}_{i;j,m,l}$ as the solution at SP (j,m,l) in cell i, where $j,m,l=1\sim(k+1)$, the solution polynomial can be constructed via the tensor product,

$$\breve{\mathbf{Q}}_i(\xi,\eta,\zeta)=\sum_{l=1}^{k+1}\sum_{m=1}^{k+1}\sum_{j=1}^{k+1}\breve{\mathbf{Q}}_{i;j,m,l}L_j(\xi)L_m(\eta)L_l(\zeta). \tag{2.4}$$

Here $L_j(\xi),L_m(\eta)$ and $L_l(\zeta)$ are the 1D Lagrange polynomials along ξ,η and ζ direction, respectively. For brevity, the subscript i indicating cells is neglected below. The flux value at each SP can be computed from the conservative variables, then the flux polynomial inside the cell can be constructed similarly,

$$\breve{\mathbf{F}}^{\xi}(\xi,\eta,\zeta)=\sum_{l=1}^{k+1}\sum_{m=1}^{k+1}\sum_{j=1}^{k+1}\breve{\mathbf{F}}^{\xi}_{j,m,l}L_j(\xi)L_m(\eta)L_l(\zeta), \tag{2.5}$$

$\breve{\mathbf{F}}^{\eta}(\xi,\eta,\zeta)$ and $\breve{\mathbf{F}}^{\zeta}(\xi,\eta,\zeta)$ have the same form as Eq. (2.5).

Since the flux polynomial is generally discontinuous across cell interfaces, the common flux needs to be computed at FP at cell interfaces to correct the above flux polynomial, such as $\breve{\mathbf{F}}^{\xi_L}_{com,m,l}$ and $\breve{\mathbf{F}}^{\xi_R}_{com,m,l}$ in the ξ direction. Here ξ_R and ξ_L indicate the FP at $(1,\eta_m,\zeta_l)$ and $(-1,\eta_m,\zeta_l)$, respectively. The correction procedure is implemented along each direction respectively according to the 1D FR approach. For example, the corrected flux polynomial along ξ direction can be obtained through

$$\begin{aligned}\breve{\mathbf{F}}^{\xi,C}(\xi,\eta_m,\zeta_l)=&\sum_{j=1}^{k+1}\breve{\mathbf{F}}^{\xi}_{j,m,l}L_j(\xi)+(\breve{\mathbf{F}}^{\xi_L}_{com,m,l}-\breve{\mathbf{F}}^{\xi_L}_{m,l})h_L(\xi)\\&+(\breve{\mathbf{F}}^{\xi_R}_{com,m,l}-\breve{\mathbf{F}}^{\xi_R}_{m,l})h_R(\xi),\end{aligned} \tag{2.6}$$

where the superscript C indicates correction, $h_L(\xi)$ and $h_R(\xi)$ are the left and right correction functions. Many well-known methods, such as DG, SD and SV, can be recovered

by choosing different correction functions. The correction function corresponding to the DG method is adopted in the present study. By taking derivative of Eq. (2.6), we have

$$\frac{\partial \check{\mathbf{F}}^{\xi,C}(\xi,\eta_m,\zeta_l)}{\partial \xi}=\sum_{j=1}^{k+1}\check{\mathbf{F}}^{\xi}_{j,m,l}\frac{L_j(\xi)}{\partial \xi}+(\check{\mathbf{F}}^{\xi_L}_{com,m,l}-\check{\mathbf{F}}^{\xi_L}_{m,l})\frac{h_L(\xi)}{\partial \xi}$$
$$+(\check{\mathbf{F}}^{\xi_R}_{com,m,l}-\check{\mathbf{F}}^{\xi_R}_{m,l})\frac{h_R(\xi)}{\partial \xi}. \tag{2.7}$$

The corrections along η and ζ direction are similar, and $\partial\check{\mathbf{F}}^{\eta,C}(\xi_j,\eta,\zeta_l)/\partial\eta$ and $\partial\check{\mathbf{F}}^{\zeta,C}(\xi_j,\eta_m,\zeta)/\partial\zeta$ can be obtained.

Finally, by taking the coordinate (ξ_j,η_m,ζ_l) of each SP into Eq. (2.7), as well as the expressions of $\partial\check{\mathbf{F}}^{\eta,C}(\xi_j,\eta,\zeta_l)/\partial\eta$ and $\partial\check{\mathbf{F}}^{\zeta,C}(\xi_j,\eta_m,\zeta)/\partial\zeta$, the semi-discrete CPR framework for updating the solution at each SP can be obtained

$$\frac{\partial \check{\mathbf{Q}}_{j,m,l}}{\partial t}=-\left(\frac{\partial \check{\mathbf{F}}^{\xi,C}_{j,m,l}}{\partial \xi}+\frac{\partial \check{\mathbf{F}}^{\eta,C}_{j,m,l}}{\partial \eta}+\frac{\partial \check{\mathbf{F}}^{\zeta,C}_{j,m,l}}{\partial \zeta}\right). \tag{2.8}$$

For the convenience of further description, Eq. (2.8) in physical space is simply written as

$$\frac{\partial \mathbf{Q}_{j,m,l}}{\partial t}=-\frac{1}{|J|_{j,m,l}}\left(\frac{\partial \check{\mathbf{F}}^{\xi,C}_{j,m,l}}{\partial \xi}+\frac{\partial \check{\mathbf{F}}^{\eta,C}_{j,m,l}}{\partial \eta}+\frac{\partial \check{\mathbf{F}}^{\zeta,C}_{j,m,l}}{\partial \zeta}\right)\equiv\mathcal{R}_{j,m,l}(\mathbf{F}(\mathbf{Q})). \tag{2.9}$$

The above-mentioned flux evaluation is conducted in the physical space, using the gas-kinetic flux solver to obtain $\mathbf{F}(\mathbf{Q})$ at SP and FP with the reconstructed conservative variables and their spatial slopes which will be introduced in the following. Subsequently all flux values are transformed into the standard element in the computational space $\check{\mathbf{F}}(\mathbf{Q})$ through Eq. (2.3) for the construction of the flux polynomial Eq. (2.5) as well as the corrected flux polynomial Eq. (2.6). Finally the conservative variables can be updated through the two-stage procedure based on Eq. (2.9) which will also be described below. In addition, the Lagrange function L_j and correction functions h_L and h_R are all known polynomials, whose derivatives can be obtained analytically and simply, thus the computation of the flux derivatives in Eq. (2.9) is straightforward.

Compared to traditional FV GKS, the current scheme can implement fourth-order compact reconstruction easily and efficiently based on the above CPR framework, which avoids the difficulty of compactness. Moreover, with the isoparametric transformation, the current scheme can handle the curved boundaries naturally. More details of the CPR framework can be found in [11–13].

2.2 Two stage gas-kinetic flux evolution

In the current scheme, the CPR framework is combined with the two-stage gas-kinetic flux evolution. The foundation is the second-order gas-kinetic flux solver, which is briefly

introduced. In the mesoscopic gas-kinetic theory, the flow can be described by the gas distribution function $f=f(\mathbf{x},t,\mathbf{u},\boldsymbol{\xi})$ which is a function of physical space $\mathbf{x}$, time t, particle velocity $\mathbf{u}=(u,v,w)$ and internal degrees of freedom $\boldsymbol{\xi}$. By taking moments of f in the phase space, the macroscopic conservative variables $\mathbf{Q}$ and the flux vector $\mathbf{F}$ can be obtained,

$$\mathbf{Q}=\int f\boldsymbol{\psi}\mathrm{d}\Xi, \tag{2.10}$$

$$\mathbf{F}=\int \mathbf{u}f\boldsymbol{\psi}\mathrm{d}\Xi, \tag{2.11}$$

where $\boldsymbol{\psi}=\left(1,\mathbf{u},(\mathbf{u}^2+\boldsymbol{\xi}^2)/2\right)^T$ is the vector of moments, $\mathrm{d}\Xi=\mathrm{d}\mathbf{u}\mathrm{d}\boldsymbol{\xi}$ is the element of the phase space. The distribution function f is governed by the BGK equation [47]

$$\frac{\partial f}{\partial t}+\mathbf{u}\cdot\nabla f=\frac{g-f}{\tau}, \tag{2.12}$$

where $\tau=\mu/p$ is the collision time, in which μ is the dynamic viscous coefficient and p is the pressure. The equilibrium state g is the Maxwellian distribution,

$$g=\rho(2\pi RT)^{-(K+3)/2}\mathrm{e}^{-[(\mathbf{u}-\mathbf{U})^2+\boldsymbol{\xi}^2]/(2RT)}, \tag{2.13}$$

where ρ is the density, R is the gas constant and T is the temperature. $K=(5-3\gamma)/(\gamma-1)$ is the total number of $\boldsymbol{\xi}$ in which γ is the specific heat ratio. By taking moments of Eq. (2.12), and considering the first-order Chapman-Enskog (C-E) expansion

$$f=g-\tau\left(\frac{\partial g}{\partial t}+\mathbf{u}\cdot\nabla g\right), \tag{2.14}$$

the Naiver-Stokes equations can be recovered. Through the zeroth order C-E expansion $f=g$, the Euler equations can be recovered.

The BGK equation has the following local analytical solution

$$f(\mathbf{x},t,\mathbf{u},\boldsymbol{\xi})=\frac{1}{\tau}\int_0^t g(\mathbf{x}-\mathbf{u}(t-t'),t',\mathbf{u},\boldsymbol{\xi})\mathrm{e}^{-(t-t')/\tau}\mathrm{d}t'+\mathrm{e}^{-t/\tau}f_0(\mathbf{x}-\mathbf{u}t,\mathbf{u},\boldsymbol{\xi}), \tag{2.15}$$

which is the foundation of constructing a time-dependent gas distribution function. f_0 is the piecewise continuous initial distribution function at the start of each time step, g is the local equilibrium state. Since the reconstructed solution is generally discontinuous across each cell interface, the gas distribution function is constructed with the solutions from both sides of a cell interface, and then the common flux can be obtained. For convenience, the cell interface is simply assumed to be perpendicular to the x-axis. Through a first-order Taylor expansion at a FP, the time-dependent gas distribution function can be

obtained

$$\begin{aligned} f_{\text{FP}}(t,\mathbf{u},\boldsymbol{\xi}) =& g_0\left(1-\mathrm{e}^{-t/\tau}+((t+\tau)\mathrm{e}^{-t/\tau}-\tau)(\mathbf{a}\cdot\mathbf{u})\right) \\ &+g_0\left((t-\tau+\tau\mathrm{e}^{-t/\tau})A\right) \\ &+\mathrm{e}^{-t/\tau}g_0^L\left(1-(\tau+t)(\mathbf{a}^L\cdot\mathbf{u})-\tau A^L\right)\mathrm{H}(u) \\ &+\mathrm{e}^{-t/\tau}g_0^R\left(1-(\tau+t)(\mathbf{a}^R\cdot\mathbf{u})-\tau A^R\right)(1-\mathrm{H}(u)), \end{aligned} \tag{2.16}$$

where $\mathrm{H}(u)$ is the Heaviside function. The coefficients $\mathbf{a}$ and A are related to the spatial and temporal slopes of the Maxwellian functions determined by the corresponding macroscopic conservative variables and their spatial derivatives. The subscript 0 represents the cell interface $x=0$ and the superscripts L,R correspond to left and right side of the interface, respectively. More details can be found in [20,21].

Since the solution is continuous inside each cell, the gas distribution function can be simplified as

$$f_{\text{SP}}(t,\mathbf{u},\boldsymbol{\xi}) = g_0(1-\tau(\mathbf{a}\cdot\mathbf{u})+(t-\tau)A), \tag{2.17}$$

which is used to determine the macroscopic flux at SP, and the computational cost is significantly reduced compared to the flux evaluation at FP. It should be noted that in these fluxes the viscous and inviscid effects are coupled and can be computed uniformly. Besides, both normal and tangential spatial derivatives are included in the gas distribution function, describing a multidimensional transport process across the cell interface, which makes it a genuinely multidimensional flux solver.

With the time-dependent gas distribution function Eqs. (2.16) and (2.17), a time-evolving flux function $\mathbf{F}(\mathbf{Q}^n,t)$ can be obtained through Eq. (2.11), in which both the flux and its time derivative are available. The efficient S2O4 temporal discretization [31,32] can therefore be adopted to achieve fourth-order time accuracy. In S2O4 scheme, the solution $\mathbf{Q}$ of Eq. (2.9) is updated by

$$\begin{aligned} \mathbf{Q}^*_{j,m,l} &= \mathbf{Q}^n_{j,m,l}+\frac{1}{2}\Delta t\mathcal{R}_{j,m,l}(\mathbf{F}^n)+\frac{1}{8}\Delta t^2\partial_t\mathcal{R}_{j,m,l}(\mathbf{F}^n), \\ \mathbf{Q}^{n+1}_{j,m,l} &= \mathbf{Q}^n_{j,m,l}+\Delta t\mathcal{R}_{j,m,l}(\mathbf{F}^n)+\frac{1}{6}\Delta t^2\left(\partial_t\mathcal{R}_{j,m,l}(\mathbf{F}^n)+2\partial_t\mathcal{R}_{j,m,l}(\mathbf{F}^*)\right), \end{aligned} \tag{2.18}$$

where $\mathbf{F}^*=\mathbf{F}(\mathbf{Q}^*,t)$ is the flux at the middle stage $t^*=t^n+\Delta t/2$. It has been proved that the two-stage temporal discretization achieves fourth-order time accuracy for hyperbolic conservation law. If the computational mesh does not change with time, $\mathcal{R}$ is a linear function of $\mathbf{F}$, we have $\partial_t\mathcal{R}(\mathbf{F})=\mathcal{R}(\partial_t\mathbf{F})$. So the two-stage temporal discretization requires not only the flux but also the time-derivative of the flux.

To obtain the time-derivative of the flux, a linear function is adopted to approximate the flux function,

$$\tilde{\mathbf{F}}(\mathbf{Q}^n,t)=\mathbf{F}^n+(t-t^n)\partial_t\mathbf{F}^n. \tag{2.19}$$

To determine the coefficients $\mathbf{F}^n$ and $\partial_t \mathbf{F}^n$, the integral of $\mathbf{F}(\mathbf{Q}^n,t)$ is computed within different time intervals,

$$\begin{aligned}\frac{1}{2}\Delta t\mathbf{F}^n+\frac{1}{8}\Delta t^2\partial_t\mathbf{F}^n&=\int_{t^n}^{t^n+\Delta t/2}\mathbf{F}(\mathbf{Q}^n,t)\mathrm{d}t\equiv\widehat{\mathbf{F}}(\mathbf{Q}^n,\Delta t/2),\\ \Delta t\mathbf{F}^n+\frac{1}{2}\Delta t^2\partial_t\mathbf{F}^n&=\int_{t^n}^{t^n+\Delta t}\mathbf{F}(\mathbf{Q}^n,t)\mathrm{d}t\equiv\widehat{\mathbf{F}}(\mathbf{Q}^n,\Delta t).\end{aligned}\tag{2.20}$$

The solutions of this algebraic equations are

$$\begin{aligned}\mathbf{F}^n&=\frac{1}{\Delta t}\left(4\widehat{\mathbf{F}}(\mathbf{Q}^n,\Delta t/2)-\widehat{\mathbf{F}}(\mathbf{Q}^n,\Delta t)\right),\\ \partial_t\mathbf{F}^n&=\frac{4}{\Delta t^2}\left(\widehat{\mathbf{F}}(\mathbf{Q}^n,\Delta t)-2\widehat{\mathbf{F}}(\mathbf{Q}^n,\Delta t/2)\right).\end{aligned}\tag{2.21}$$

The coefficients $\mathbf{F}^*$ and $\partial_t\mathbf{F}^*$ can be obtained similarly through the above-mentioned linear approximation based on $\mathbf{Q}^*$.

Then substituting these coefficients in Eq. (2.18) and considering the linearity of $\mathcal{R}$ with flux $\mathbf{F}$, the conservative variables can be updated through the first stage,

$$\mathbf{Q}^*_{j,m,l}=\mathbf{Q}^n_{j,m,l}+\mathcal{R}_{j,m,l}(\widetilde{\mathbf{F}}),\tag{2.22}$$

where

$$\widetilde{\mathbf{F}}=\widehat{\mathbf{F}}(\mathbf{Q}^n,\Delta t/2),\tag{2.23}$$

and the second stage,

$$\mathbf{Q}^{n+1}_{j,m,l}=\mathbf{Q}^*_{j,m,l}+\mathcal{R}_{j,m,l}(\widetilde{\mathbf{F}}^*),\tag{2.24}$$

where

$$\widetilde{\mathbf{F}}^*=\frac{8}{3}\widehat{\mathbf{F}}(\mathbf{Q}^n,\Delta t/2)-\frac{1}{3}\widehat{\mathbf{F}}(\mathbf{Q}^n,\Delta t)-\frac{8}{3}\widehat{\mathbf{F}}(\mathbf{Q}^*,\Delta t/2)+\frac{4}{3}\widehat{\mathbf{F}}(\mathbf{Q}^*,\Delta t).\tag{2.25}$$

The two-stage gas-kinetic CPR method is summarized as below. At the first stage $[t^n,t^*]$, with the solution at t^n, we can construct the gas distribution function at each FP and SP respectively through Eqs. (2.16) and (2.17), so that the time integrals $\widehat{\mathbf{F}}(\mathbf{Q}^n,\Delta t/2)$ and $\widehat{\mathbf{F}}(\mathbf{Q}^n,\Delta t)$ can be computed. Then the solution at each SP is updated by Eq. (2.22).

At the second stage $[t^*,t^{n+1}]$, with the solution at t^*, the time integrals $\widehat{\mathbf{F}}(\mathbf{Q}^*,\Delta t/2)$ and $\widehat{\mathbf{F}}(\mathbf{Q}^*,\Delta t)$ can be computed at each SP and FP, similar to the first stage. Thus the conservative variables at t^{n+1} for each SP can be obtained by Eq. (2.24).

More details can be found in [36]. It has been proved that the two-stage temporal discretization achieves fourth-order time accuracy for hyperbolic conservation law. For traditional CPR methods, the four-stage or five-stage R-K method is needed to achieve fourth-order time accuracy. In contrast, only two stages are required in the current CPR-GKS. Besides, the additional treatment for viscous terms is avoided since the inviscid and viscous fluxes are coupled in the gas-kinetic flux. As a result, the current scheme is expected to be more efficient than traditional CPR methods for solving viscous flow problems.

3 Numerical tests

Several benchmark numerical cases are simulated to validate the performance of the current CPR-GKS. The collision time for viscous flows is given by

$$\tau=\frac{\mu}{p},\quad \tau_n=\frac{\mu}{p}+\epsilon_2\left|\frac{p^L-p^R}{p^L+p^R}\right|\Delta t. \tag{3.1}$$

in which τ is the physical collision time, while τ_n is the numerical collision time for replacing τ in the exponential function in Eq. (2.15) so that the numerical dissipation can be better controlled through the transition from f_0 to g. p^L and p^R are the pressure at the left and right sides of a cell interface. ϵ_2 is fixed to 10. For inviscid flows, we set $\tau=0$ to approximate the inviscid assumption, and μ/p in τ_n is replaced with $\epsilon_1\Delta t$ to provide necessary numerical dissipation, where $\epsilon_1=0.05$. The ratio of specific heats is $\gamma=1.4$ in all of these tests. To compute the time step Δt based on the mesh size h, the CFL number is set as 0.04, which corresponds to 0.28 after multiplying the factor $2k+1=7$ with $k=3$ for the degree of polynomials [48]. We note that only subsonic flows are considered in the present study. According to our preliminary tests, the CFL number can be higher, such as 0.1, when simulating high-speed flows. Further study on high-speed flows, especially for shock capturing will be carried out in the near future.

3.1 Advection of density perturbation

The 3D advection of density perturbation has the following analytical solution

$$\begin{aligned}&\rho(\mathbf{x},t)=1+0.2\sin(c(x-t))\sin(c(y-t))\sin(c(z-t)),\\&U(\mathbf{x},t)=V(\mathbf{x},t)=W(\mathbf{x},t)=1,\\&p(\mathbf{x},t)=1.\end{aligned} \tag{3.2}$$

$c=0.2\pi$ is chosen and the flow field is initialized with $t=0$. The computational domain is $[0,10]\times[0,10]\times[0,10]$. The computational mesh with $h=2$ is shown in Fig. 3. The periodic boundary condition is imposed on all boundaries. The density error is between the numerical and analytical solutions is adopted to evaluate the accuracy of CPR-GKS, which is computed by

$$\mathrm{L}_2\text{ error}=\sqrt{\frac{\sum_{i=1}^{N}\int_{\Omega_i}(\rho_i-\rho_i^e)^2\mathrm{d}\Omega}{\sum_{i=1}^{N}|\Omega_i|}}, \tag{3.3}$$

in which the subscript i denote the cell i and the superscript e the analytical solution. N is the number of cells. $|\Omega_i|$ is the volume of cell i. The results at $t=10$ are shown in Table 1, which shows that the designed fourth-order accuracy can be achieved. Besides, compared to the results presented in [43], the computational errors are much lower than SCFV-GKS with the same mesh size.

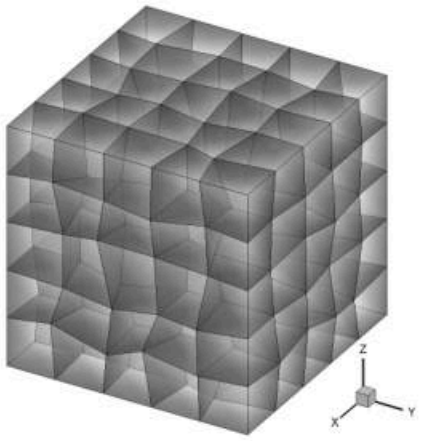

Figure 3: Sample mesh for advection of density perturbation.

Table 1: Accuracy test in the advection of density perturbation.

Grid size	L_2 error	Order
$5\times5\times5$	1.56E-04	
$10\times10\times10$	9.66E-06	4.01
$20\times20\times20$	6.15E-07	3.97
$40\times40\times40$	3.89E-08	3.98
$80\times80\times80$	2.44E-09	3.99

3.2 Compressible Couette flow

To validate the accuracy and efficiency in viscous flows, the compressible Couette flow is tested, which has an analytical solution [20, 30]. It is a steady flow between two parallel plates, driven by the upper plate, which has a constant speed $U_1=0.5$ and temperature $T_1=1$. The lower plate is stationary and adiabatic. The computational domain is $[0,4H]\times[0,2H]\times[0,H]$ with $H=1$. The Mach number is set as $\mathrm{Ma}=U_1/\sqrt{\gamma RT_1}=0.5$ and the Reynolds number is $\mathrm{Re}=\rho_1U_1H/\mu_1=500$ with $\rho_1=1$. The viscosity of the flow is determined by the linear law $\mu=\mu_1T/T_1$. The Prandtl number is $\mathrm{Pr}=1$. The flow variables at ghost cells are fixed to the analytical solutions for all boundaries.

For comparison, the results obtained by the traditional CPR method (denoted as CPR-LDG) is also presented, in which the inviscid flux is computed by the Rusanov scheme, while the viscous flux is computed by the LDG scheme. The five-stage fourth-order R-K method is used for time stepping. The errors and convergence orders of density are presented in Table 2. Both of the two schemes achieve the designed order of accuracy. The errors of CPR-GKS is slightly smaller than that of CPR-LDG. Table 3 shows the computational cost for $t=300$ with the coarsest mesh, in which T_{SP} and T_{FP} indicate the cost of

Table 2: Accuracy test in the compressible Couette flow.

Grid size	CPR-GKS		CPR-LDG	
	L_2 error	Order	L_2 error	Order
$4\times2\times1$	1.87E-06		2.23E-06	
$8\times4\times2$	1.16E-07	4.02	1.55E-07	3.85
$16\times8\times4$	7.20E-09	4.01	9.45E-09	4.04
$32\times16\times8$	4.51E-10	4.00	5.85E-10	4.01

Table 3: Computational cost for $t=300$ with the coarsest mesh.

Scheme	T_{SP}	T_{FP}	T_{others}	T_{total}
CPR-GKS	22.39	49.2	58.21	129.8
CPR-LDG	22.93	34.69	177.58	235.2

flux evaluation at SP and FP respectively. As can be seen, CPR-GKS has higher efficiency than CPR-LDG since only two stages are required within a time step and there is no need to compute viscous flux additionally.

3.3 Inviscid flow over a sphere

In order to validate the capability of CPR-GKS in handling curved boundaries, the steady inviscid flow over a sphere is simulated. The freestream Mach number is $\mathrm{Ma}=0.1$. To better approximate the geometry of the sphere, cubic isoparametric elements are used, which means the curved boundary face is represented with piecewise cubic polynomials.

The computational mesh is shown in Fig. 4, in which only elements with $y>0$ are presented for better illustration. The radius of the sphere is 0.5. The outer boundary is also spherical, which has the radius of 5. There are 16 elements uniformly distributed

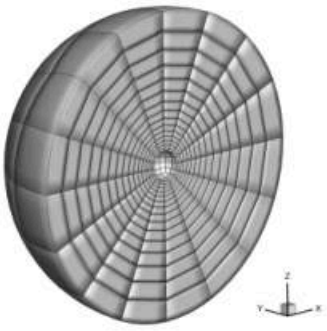

Figure 4: Computational mesh in the inviscid flow over a sphere.

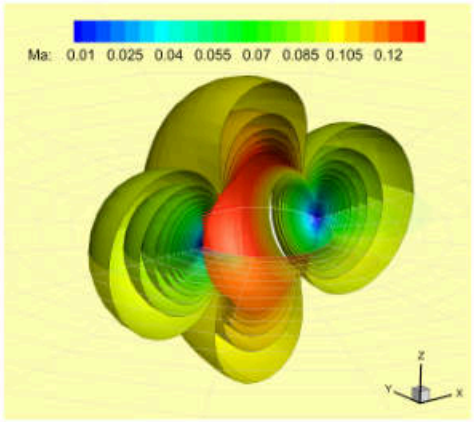

Figure 5: 3D iso-surface of the Mach number in the inviscid flow over a sphere.

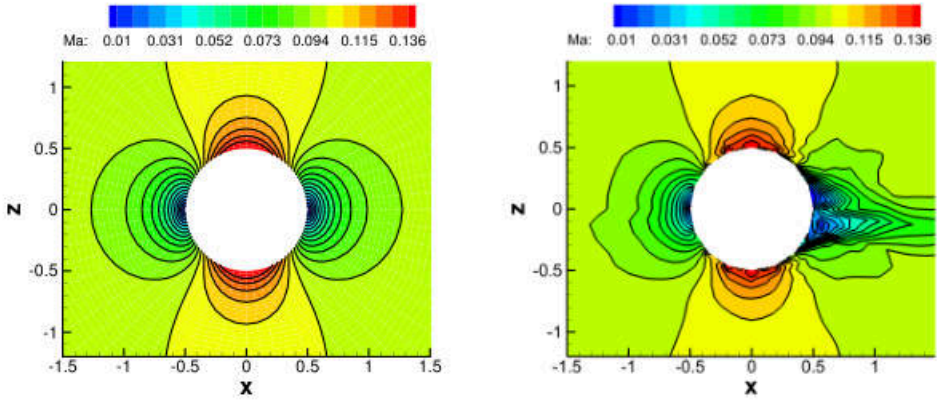

Figure 6: 2D contours of the Mach number at the plane $y=0$ with cubic mesh (left) and linear mesh (right) in the inviscid flow over a sphere.

along the circumferential direction and 15 in the radial direction with minimum cell size 0.094 near the wall. The reflecting boundary condition is imposed on the sphere wall, while the characteristic boundary condition is set on the outer boundary. The steady state is achieved when the residual of density is less than 10^{-13}.

The 3D iso-surface of the Mach number is shown in Fig. 5. The predicted flow is smooth and the symmetry is well preserved. Fig. 6 presents the 2D contours at the plane $y=0$ computed on both cubic and linear mesh. It can be observed that, with the linear mesh, non-physical results occur behind the sphere. The results indicate the importance of the consistence between computational mesh and physical curved boundaries for high order schemes. If simply using linear mesh, large errors may arise near the boundary and the solutions inside the computational domain can also be polluted.

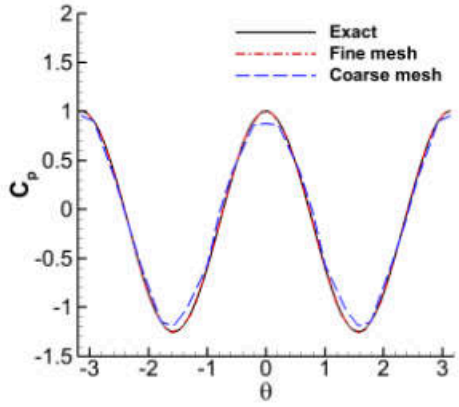

Figure 7: Pressure coefficient on the sphere at the plane $y=0$.

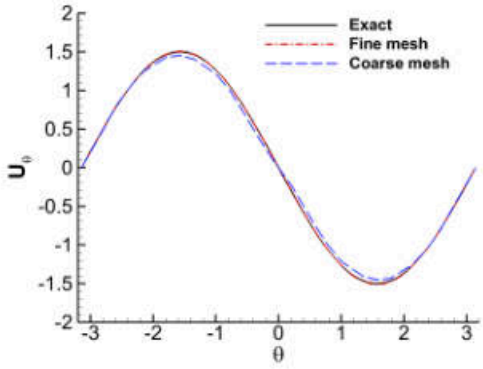

Figure 8: Tangential velocity on the sphere at the plane $y=0$.

Besides, Figs. 7 and 8 present the computed pressure coefficient and the tangential velocity on the sphere at the plane $y=0$, labeled as fine mesh. For the tangential velocity, the anti-clockwise direction is the positive direction. It can be observed that the predicted results match very well with the exact solutions. A coarse mesh are also considered for comparison in which only 8 elements are adopted along both circumferential and radial directions, and the minimum radial cell size is 0.359. The coarse-mesh results also achieve a good agreement with the exact solutions, except for the solutions near the extreme points.

3.4 Viscous flow over a sphere

To verify the performance of the current scheme in unsteady viscous flows, the viscous flow over a sphere is simulated with $\mathrm{Re}=300$ which is based on the diameter of the

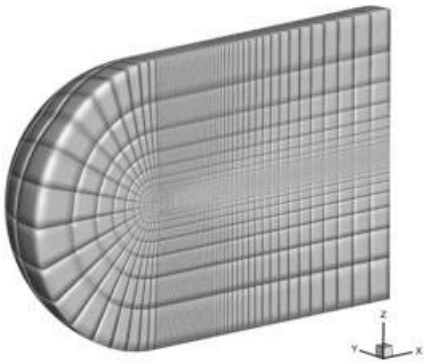

Figure 9: Computational mesh in the viscous flow over a sphere.

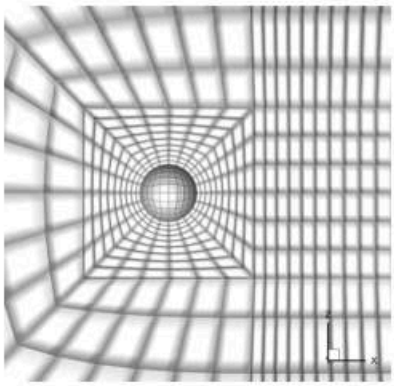

Figure 10: Zoom-in mesh near the sphere in the viscous flow over a sphere.

sphere. The diameter is set as 1. The freestream Mach number is $\mathrm{Ma}=0.3$. The computational mesh is shown in Fig. 9, in which only elements with $y>0$ are presented. The zoom-in mesh near the sphere is shown in Fig. 10. The cubic isoparametric elements are also used to handle the curved boundary. The minimum radial mesh size is near the wall with value 0.076. The total number of hexahedral elements is 20304. The outer boundary is consisted of a half sphere surface with the radius of 50 and a cylindrical surface with the length of 100. The non-slip adiabatic boundary condition is imposed on the sphere wall, while the characteristic boundary condition is imposed on the outer boundary.

Fig. 11 shows the iso-surface of the Q-criterion at $t=519$, besides, the 2D contours of the Mach number at the plane $y=0$ are also presented. As can be seen, the unsteady shedding of the hairpin vortex is well captured. The time history of the lift and drag coefficients is shown in Fig. 12. Table 4 presents the time-averaged values of the lift and drag coefficients over 10 periods, as well as the Strouhal number. The current results match well with the reference values.

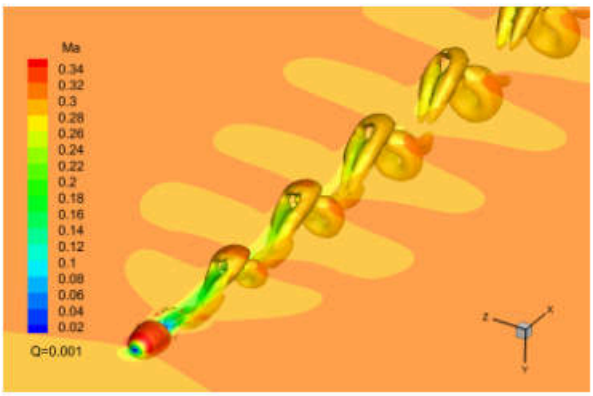

Figure 11: Iso-surface of the Q-criterion at $t=300$ in the viscous flow over a sphere.

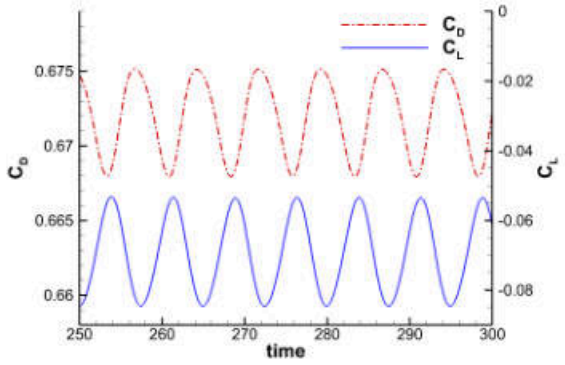

Figure 12: Time history of the lift and drag coefficients in the viscous flow over a sphere.

Table 4: Time-averaged lift and drag coefficients over 10 periods and the Strouhal number

	$\bar{C}_L$	$\bar{C}_D$	St
Present	-0.069	0.672	0.133
Haga et al. [16]	–	0.670	0.131
Gassner [49]	-0.065	0.673	0.135
Johnson and Patel [50]	-0.069	0.656	0.137

3.5 Taylor–Green vortex

This case is tested to validate the performance of high-order methods on the direct numerical simulation of a three-dimensional periodic and transitional flow defined by a simple initial condition, i.e. the Taylor–Green vortex. The initial condition is given

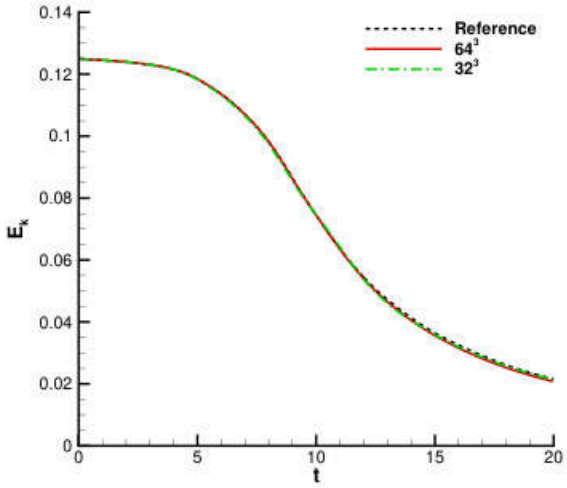

Figure 13: Temporal evolution of the kinetic energy in the Taylor–Green vortex with Ma = 0.1.

by [51],

$$\begin{aligned}
&U(x,y,z) = U_0 \sin\left(\frac{x}{L}\right)\cos\left(\frac{y}{L}\right)\cos\left(\frac{z}{L}\right),\\
&V(x,y,z) = -U_0 \cos\left(\frac{x}{L}\right)\sin\left(\frac{y}{L}\right)\cos\left(\frac{z}{L}\right),\\
&W(x,y,z) = 0,\\
&p(x,y,z) = p_0 + \frac{\rho_0 U_0^2}{16}\left(\cos\left(\frac{2x}{L}\right)+\cos\left(\frac{2y}{L}\right)\right)\left(\cos\left(\frac{2z}{L}\right)+2\right).
\end{aligned} \tag{3.4}$$

The computational domain is $-\pi L \leqslant x,y,z \leqslant \pi L$. The periodical condition is applied to all boundaries. Two computational meshes are adopted with 32^3 and 64^3 hexahedral elements respectively. The Reynolds number is set as $\mathrm{Re} = \rho_0 U_0 L/\mu = 1600$, in which $\rho_0 = 1$, $U_0 = 1$, $L = 1$, and the dynamic viscosity μ is computed through the Sutherland law. The Prandtl number is $\mathrm{Pr} = 0.71$.

Firstly, the incompressible case is tested with the Mach number $\mathrm{Ma} = U_0/\sqrt{\gamma p_0/\rho_0} = 0.1$. Figs. 13 and 14 present the temporal evolution of the kinetic energy E_k and the corresponding total dissipation rate $-\mathrm{d}E_k/\mathrm{d}t$. The results obtained on the mesh 64^3 match very well with the reference data [51] for both E_k and $-\mathrm{d}E_k/\mathrm{d}t$, which is obtained by a 13-point dispersion-relation-preserving (DRP) scheme with 512^3 grid points. Furthermore, a comparison between the current scheme and traditional high-order schemes is made in terms of the enstrophy based dissipation rate

$$\varepsilon_s = \frac{1}{\rho_0 \mathrm{Re}}\int_\Omega \mu(\nabla\times\mathbf{U})^2 \mathrm{d}\Omega, \tag{3.5}$$

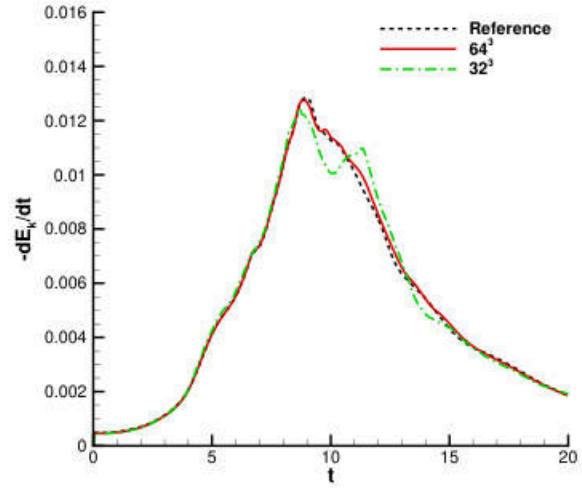

Figure 14: Temporal evolution of the total dissipation rate based on the kinetic energy in the Taylor–Green vortex with $\mathrm{Ma}=0.1$.

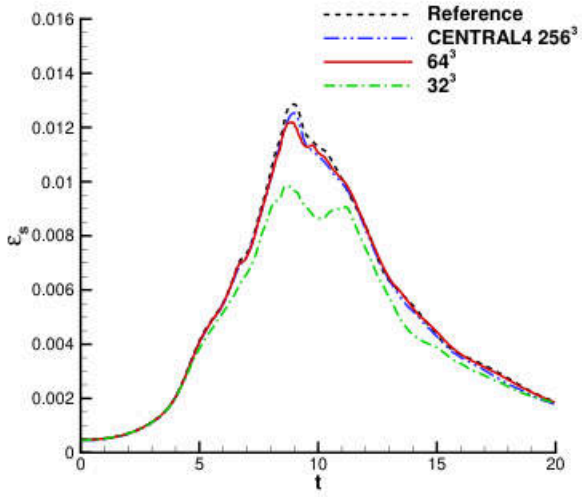

Figure 15: Comparison of the dissipation rate based on the enstrophy in the Taylor–Green vortex with $\mathrm{Ma}=0.1$.

which is more challenging to predict. Since the current scheme contains 4^3 IDOFs inside each cell, the result obtained on the mesh 64^3 should be compared with the results obtained by traditional schemes on the mesh 256^3 for fairness. As shown in Fig. 15, the predicted results agree well with those from a non-dissipative fourth-order central scheme with 256^3 grid points [52], demonstrating the high accuracy of the current scheme. More-

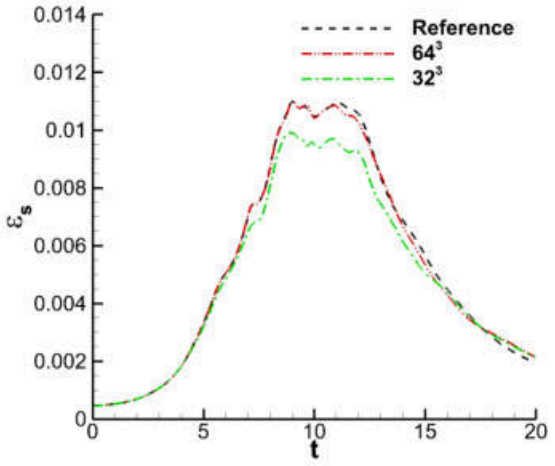

Figure 16: Dissipation rate based on the enstrophy in the Taylor–Green vortex with Ma = 0.75.

over, compared to the results shown in [43], the current result obtained on the mesh 64^3 is also more accurate than that obtained by SCFV-GKS on the grid 128^3 cells, which contains 256^3 DOFs as well. This mainly comes from the discontinuities introduced between sub-cells for SCFV. The superiority of the current scheme for smooth flows is demonstrated again. Secondly, a compressible case with Ma = 0.75 is tested. The enstrophy based dissipation rate is shown in Fig. 16, in which the results obtained on the mesh 64^3 also match well with the reference data [52]. Besides, Figs. 17 and 18 shows the iso-surface of the Q-criterion at $t = 10$ with Ma = 0.1 and 0.75 respectively. The complex flow structures are well captured.

4 Conclusions

A fourth-order gas-kinetic CPR method is developed for 3D subsonic inviscid and viscous flows on hexahedral meshes. The developed scheme combines the compact and efficient CPR framework with the robust and time-evolving gas-kinetic flux, as well as an efficient two-stage fourth-order temporal discretization. Compared to traditional high-order finite volume GKS, the difficulty of compact fourth-order reconstruction is avoided based on the CPR framework. Moreover, the current scheme can treat curved boundaries more accurately and easily with the help of iso-parametric transformation. On the other hand, different from traditional Runge-Kutta CPR method, the current CPR-GKS fully takes advantage of the unique features of the gas-kinetic flux. The inviscid and viscous fluxes are coupled and obtained uniformly. The gas distribution function takes both the normal and tangential space derivatives into account, which is genuinely multi-dimensional. More importantly, the time-evolving gas-kinetic flux provides both the flux

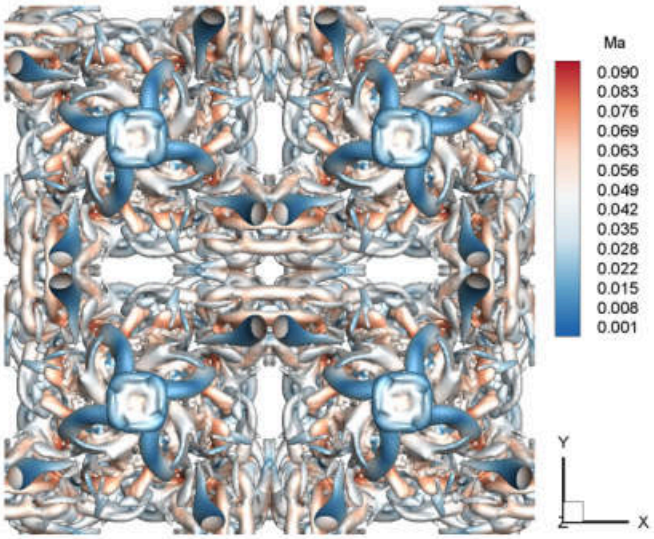

Figure 17: Iso-surface of the Q-criterion colored by velocity magnitude at $t=10$ in the Taylor–Green vortex with $\mathrm{Ma}=0.1$.

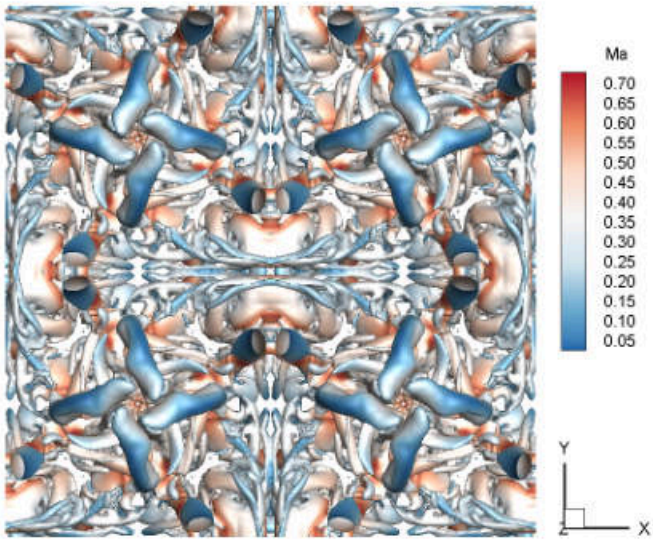

Figure 18: Iso-surface of the Q-criterion colored by velocity magnitude at $t=10$ in the Taylor–Green vortex with $\mathrm{Ma}=0.75$.

and its time-derivatives so that the two-stage fourth-order temporal discretization can be extended to the CPR framework, which is more efficient than the multi-stage Runge-Kutta method by avoiding the computational cost of additional stages. Numerical tests demonstrate that the current scheme can achieve fourth order accuracy in space and time, and performs well in both inviscid and viscous flows with curved boundaries.

The present study focuses on numerical methods for subsonic flow where shock waves are absent. For supersonic flow simulations, limiting procedure is necessary to capture strong flow discontinuities which is a great challenge for a high-order accurate scheme with inner degrees of freedom. The subcell finite volume limiting procedure can be adopted which has shown good robustness and accuracy under CPR framework on triangular meshes [53]. In the future study, this limiting method can be extended to hexahedral meshes to develop a new CPR method for 3D high-speed complex flows, such as the reentry flows around irregular disintegrations.

Acknowledgments

This work is supported by the National Natural Science Foundation of China (12372218, 91852109) and National Key Basic Research and Development Program (2014CB744100). We also would like to acknowledge the technical support of PARATERA.

References

[1] Z. Han, Z. Li, Z. Bai, X. Li, J. Zhang, Study on numerical algorithm of the N-S equation for multi-body flows around irregular disintegrations in near space, Aerosp. 9 (2022) 347.
[2] B. Cockburn, C.-W. Shu, The Runge-Kutta discontinuous Galerkin method for conservation laws V: Multidimensional systems, J. Comput. Phys. 141 (1998) 199–224.
[3] H. Luo, J. Baum, R. Lohner, A discontinuous Galerkin method based on a Taylor basis for the compressible flows on arbitrary grids, J. Comput. Phys. 227 (2008) 8875–8893.
[4] X. Zhang, C.-W. Shu, On positivity-preserving high order discontinuous Galerkin schemes for compressible Euler equations on rectangular meshes, J. Comput. Phys. 229 (2010) 8918–8934.
[5] Y. Liu, M. Vinokur, Z. J. Wang, Spectral difference method for unstructured grids I: Basic formulation, J. Comput. Phys. 216 (2006) 780–801.
[6] C. Liang, A. Jameson, Z. J. Wang, Spectral difference method for compressible flow on unstructured grids with mixed elements, J. Comput. Phys. 228 (2009) 2847–2858.
[7] Z. J. Wang, Spectral (finite) volume method for conservation laws on unstructured grids: Basic formulation, J. Comput. Phys. 178 (2002) 210–251.
[8] Z. J. Wang, L. Zhang, Y. Liu, Spectral (finite) volume method for conservation laws on unstructured grids IV: Extension to two-dimensional systems, J. Comput. Phys. 194 (2) (2004) 716–741.
[9] T. J. Barth, P. O. Frederickson, Higher order solution of the Euler equations on unstructured grids using quadratic reconstruction, in: 28th Aerospace Sciences Meeting, AIAA Paper 1990-0013, Jan. 8-11, Reno, Nevada, 1990.

[10] C. Hu, C.-W. Shu, Weighted essentially non-oscillatory schemes on triangular meshes, J. Comput. Phys. 150 (1999) 97–127.
[11] H. T. Huynh, A flux reconstruction approach to high-order schemes including discontinuous Galerkin methods, in: 18th AIAA Computational Fluid Dynamics Conference, AIAA Paper 2007-4079, 2007.
[12] H. T. Huynh, A reconstruction approach to high-order schemes including discontinuous Galerkin for diffusion, in: 47th AIAA Aerospace Sciences Meeting Including the New Horizons Forum and Aerospace Exposition, AIAA Paper 2009-403, 2009.
[13] Z. J. Wang, H. Gao, A unifying lifting collocation penalty formulation including the discontinuous Galerkin, spectral volume/difference methods for conservation laws on mixed grids, J. Comput. Phys. 228 (2009) 8161–8186.
[14] H. Gao, Z. J. Wang, A high-order lifting collocation penalty formulation for the Navier-Stokes equations on 2-D mixed grids, in: 19th AIAA Computational Fluid Dynamics, AIAA Paper 2009-3784, 2009.
[15] T. Haga, H. Gao, Z. J. Wang, A high-order unifying discontinuous formulation for 3-D mixed grids, in: 48th AIAA Aerospace Sciences Meeting Including the New Horizons Forum and Aerospace Exposition, AIAA Paper 2010-540, 2010.
[16] T. Haga, H. Gao, Z. J. Wang, A high-order unifying discontinuous formulation for the Navier-Stokes equations on 3D mixed grids, Math. Model. Nat. Phenom. 6 (2011) 28–56.
[17] H. T. Huynh, Z. J. Wang, P. E. Vincent, High-order methods for computational fluid dynamics: A brief review of compact differential formulations on unstructured grids, Comput. Fluids 98 (2014) 209–220.
[18] V. Titarev, E. Toro, ADER: Arbitrary high order Godunov approach, J. Sci. Comput. 17 (2002) 609–618.
[19] T. Schwartzkopff, C. Munz, E. Toro, ADER: A high-order approach for linear hyperbolic systems in 2D, J. Sci. Comput. 17 (2002) 231–240.
[20] K. Xu, A gas-kinetic BGK scheme for the Navier-Stokes equations and its connection with artificial dissipation and Godunov method, J. Comput. Phys. 171 (2001) 289–335.
[21] Q. B. Li, S. Fu, K. Xu, A compressible Navier-Stokes flow solver with scalar transport, J. Comput. Phys. 204 (2) (2005) 692–714.
[22] K. Xu, M. Mao, L. Tang, A multidimensional gas-kinetic BGK scheme for hypersonic viscous flow, J. Comput. Phys. 203 (2005) 405–421.
[23] Q. B. Li, S. Fu, On the multidimensional gas-kinetic BGK scheme, J. Comput. Phys. 220 (2006) 532–548.
[24] Q. B. Li, S. Fu, A high-order accurate gas-kinetic BGK scheme, in: 5th International Conference on Computational Fluid Dynamics, July 7-11, Seoul, Korea, 2008, pp. 515–520.
[25] Q. B. Li, K. Xu, S. Fu, A high-order gas-kinetic Navier-Stokes flow solver, J. Comput. Phys. 229 (2010) 6715–6731.
[26] Q. B. Li, S. Fu, On the high-order multidimensional gas-kinetic scheme, in: 7th International Conference on Computational Fluid Dynamics, July 9-13, Big Island, Hawaii, 2012.
[27] L. Pan, K. Xu, A third-order compact gas-kinetic scheme on unstructured meshes for compressible Navier-Stokes solutions, J. Comput. Phys. 318 (2016) 327–348.
[28] X. Ren, K. Xu, W. Shyy, C. Gu, A multi-dimensional high-order discontinuous Galerkin method based on gas kinetic theory for viscous flow computations, J. Comput. Phys. 292 (2015) 176–193.
[29] N. Liu, X. Xu, Y. Chen, High-order spectral volume scheme for multi-component flows using non-oscillatory kinetic flux, Comput. Fluids 152 (2017) 120–133.

[30] C. Zhang, Q. B. Li, S. Fu, Z. J. Wang, A third-order gas-kinetic CPR method for the Euler and Navier-Stokes equations on triangular meshes, J. Comput. Phys. 363 (2018) 329–353.
[31] J. Li, Z. Du, A two-stage fourth order time-accurate discretization for Lax-Wendroff type flow solvers I. Hyperbolic conservation laws, SIAM J. Sci. Comput. 38 (5) (2016) A3046–A3069.
[32] Z. Du, J. Li, A two-stage fourth order time-accurate discretization for Lax-Wendroff type flow solvers II. High order numerical boundary conditions, J. Comput. Phys. 369 (2018) 125–147.
[33] J. Li, Two-stage fourth order: Temporal-spatial coupling in computational fluid dynamics (CFD), Adv. Aerodyn. 1 (2019) 3.
[34] J. Cheng, Z. Du, X. Lei, Y. Wang, J. Li, A two-stage fourth-order discontinuous Galerkin method based on the GRP solver for the compressible Euler equations, Comput. Fluids 181 (2019) 248–258.
[35] A. Li, J. Li, J. Cheng, C.-W. Shu, High order compact Hermite reconstructions and their application in the improved two-stage fourth order time-stepping framework for hyperbolic problems: Two-dimensional case, Commun. Comput. Phys. 36 (2024) 1–29.
[36] L. Pan, K. Xu, Q. B. Li, J. Li, An efficient and accurate two-stage fourth-order gas-kinetic scheme for the Euler and Navier-Stokes equations, J. Comput. Phys. 326 (2016) 197–221.
[37] F. Zhao, X. Ji, W. Shyy, K. Xu, Compact higher-order gas-kinetic schemes with spectral-like resolution for compressible flow simulations, Adv. Aerodyn. 1 (2019) 13.
[38] X. Ji, F. Zhao, W. Shyy, K. Xu, A family of high-order gas-kinetic schemes and its comparison with Riemann solver based high-order methods, J. Comput. Phys. 356 (2018) 150–173.
[39] J. Mu, C. Zhuo, Q. Zhang, S. Liu, C. Zhong, An efficient high-order gas-kinetic scheme with hybrid WENO-AO method for the Euler and Navier-Stokes solutions, Commun. Comput. Phys. 35 (2024) 662–692.
[40] X. Ji, W. Shyy, K. Xu, A gradient compression-based compact high-order gas-kinetic scheme on 3D hybrid unstructured meshes, J. Comput. Phys. 35 (2021) 485–509.
[41] C. Zhang, Q. B. Li, A third-order subcell finite volume gas-kinetic scheme for the Euler and Navier-Stokes equations on triangular meshes, J. Comput. Phys. 436 (2021) 110245.
[42] C. Zhang, Q. B. Li, P. Song, J. Li, Two-stage fourth-order gas kinetic solver-based compact subcell finite volume method for compressible flows on triangular meshes, Phys. Fluids 33 (2021) 126108.
[43] C. Zhang, Q. B. Li, P. Song, J. Li, Two-stage fourth-order subcell finite volume method on hexahedral meshes for compressible flows, Phys. Fluids 34 (2022) 086110.
[44] L. Krivodonova, M. Berger, High-order accurate implementation of solid wall boundary conditions in curved geometries, J. Comput. Phys. 211 (2006) 492–512.
[45] X. Ji, F. Zhao, W. Shyy, K. Xu, A HWENO reconstruction based high-order compact gas-kinetic scheme on unstructured mesh, J. Comput. Phys. 410 (2020) 109367.
[46] F. Bassi, S. Rebay, High-order accurate discontinuous finite element solution of the 2D Euler equations, J. Comput. Phys. 138 (1997) 251–285.
[47] P. Bhatnagar, E. Gross, M. Krook, A model for collision processes in gases I: Small amplitude processes in charged and neutral one-component systems, Phys. Rev. 94 (1954) 511–525.
[48] H. You, C. Kim, High-order multi-dimensional limiting strategy with subcell resolution I. two-dimensional mixed meshes, J. Comput. Phys. 375 (2018) 1005–1032.
[49] G. J. Gassner, F. Lorcher, C.-D. Munz, J. S. Hesthaven, Polymorphic nodal elements and their application in discontinuous Galerkin methods, J. Comput. Phys. 228 (2009) 1573–1590.
[50] T. A. Johnson, V. C. Pate, Flow past a sphere up to a Reynolds number of 300, J. Fluid Mech.

378 (1999) 19–70.
[51] J. Debonis, Solutions of the Taylor–Green vortex problem using high-resolution explicit finite difference methods, AIAA Paper 2013-0382, 2013.
[52] D. J. Lusher, N. D. Sandham, Assessment of low-dissipative shock-capturing schemes for the compressible Taylor–Green vortex, AIAA J. 59 (2) (2021) 662–692.
[53] C. Zhang, Q. B. Li, Z. J. Wang, J. Li, S. Fu, A two-stage fourth-order gas-kinetic CPR method for the Navier-Stokes equations on triangular meshes, J. Comput. Phys. 451 (2022) 110830.